Benchmarking Nitrous Oxide Adsorption and Activation in Metal-Organic Frameworks Bearing Coordinatively Unsaturated Metal Centers

Tristan A. Pitt,[a] Haojun Jia,[b,c] Tyler J. Azbell,[a] Mary E. Zick,[a] Aditya Nandy,[b,c] Heather J. Kulik,[b,c] Phillip J. Milner[a,*]

a. Department of Chemistry and Chemical Biology, Cornell University, Ithaca, NY, 14850, United States.
b. Department of Chemical Engineering, Massachusetts Institute of Technology, Cambridge, MA, 02139, United States.
c. Department of Chemistry, Massachusetts Institute of Technology, Cambridge, MA, 02139, United States.

Anthropogenic emissions of N_2O, the third most abundant greenhouse gas after CO_2 and CH_4, are contributing to global climate change. Although metal-organic frameworks (MOFs) have been widely studied as adsorbents for CO_2 and CH_4, less effort has focused on the use of MOFs to remove N_2O from emission streams or from air. Further, N_2O activation would enable its use as an inexpensive oxidant for fine chemical synthesis. Herein, we identify features that contribute to strong binding and high uptake of N_2O at coorinatively unsaturated metal sites in the $M_2Cl_2(btdd)$ (M= Mn, Co, Ni, Cu; $btdd^{2-}$ = bis(1,2,3-triazolo[4,5-b],[4′,5′-i])dibenzo[1,4]dioxin) and $M_2(dobdc)$ (M = Mg, Mn, Fe, Co, Ni, Cu, Zn; $dobdc^{4-}$ = 2,5-dioxido-1,4-benzenedicarboxylate) series of MOFs. Combined experimental and computational studies suggest that N_2O adsorption at open-metal-sites is primarily based on electrostatic interactions, rather than π-backbonding, causing MOFs with more Lewis acidic metal centers to be superior N_2O adsorbents. As a result, $Mg_2(dobdc)$ demonstrates strong binding and record-setting N_2O uptake (8.75 mmol/g at 1 bar and 298 K). Using density functional theory (DFT) to characterize reactive intermediates and transition states, we demonstrate that N_2O activation to form a M(IV)-oxo species and N_2 is thermodynamically favorable in $Mn_2(dobdc)$ and $Fe_2(dobdc)$ but appears to be kinetically limited in $Mn_2(dobdc)$. Our work lays a foundation for understanding N_2O adsorption and activation in MOFs, paving the way for the design of promising next-generation materials for N_2O capture and utilization.

Introduction

N_2O is the third most prevalent anthropogenic greenhouse gas after CO_2 and CH_4, accounting for 6% of the effective radiative forcing from 1960 to 2019.[1] Although CO_2 and CH_4 are present in higher concentrations in the atmosphere, the global warming potential of N_2O (265) is far greater (1 and 28 for CO_2 and CH_4, respectively) and its atmospheric lifetime (116 y) is far longer (1 and 12 y for CO_2 and CH_4, respectively).[2] Over the last four decades, global anthropogenic emissions of N_2O have increased by 30%.[3] Up to 87% of this increase derives from agricultural practices such as nitrogen additions to soils. By nature, the sources of these emissions (i.e., farmlands) are diffuse, in contrast to point sources of N_2O emissions such as adipic and nitric acid manufacturing.[4] Diffuse emissions are currently largely uncontrolled, except for preventative measures such as the use of more efficient fertilizers.[5,6] At point sources, N_2O can be catalytically destroyed, but regulations requiring this practice have not been globally adopted.[7] Thus, the majority of human-caused N_2O emissions are currently unabated, leading to a current estimated rate of increase in atmospheric N_2O concentration of 2% per decade.[3] In addition to its global warming potential, N_2O was found to be the dominant ozone-depleting substance emitted in the 21st century,[4] underscoring the urgency of curtailing N_2O emissions. The environmental effects of anthropogenic N_2O emissions and its long atmospheric lifetime necessitate the development of new materials for N_2O capture.

Selectively capturing gases from diffuse sources such as air is a unique challenge that requires specially designed sorbents. Metal-organic frameworks (MOFs) are an emerging class of materials that have drawn significant interest for their potential applications in greenhouse gas capture,[8] separations,[9] catalysis,[10] and beyond.[11] They are crystalline, highly porous materials formed by connecting metal secondary building units (SBU) with multitopic organic linkers. MOFs have been designed to selectively bind CO_2 and CH_4 based on electrostatic interactions,[12,13] chemical reactivity,[14–16] hydrogen bonding,[17]

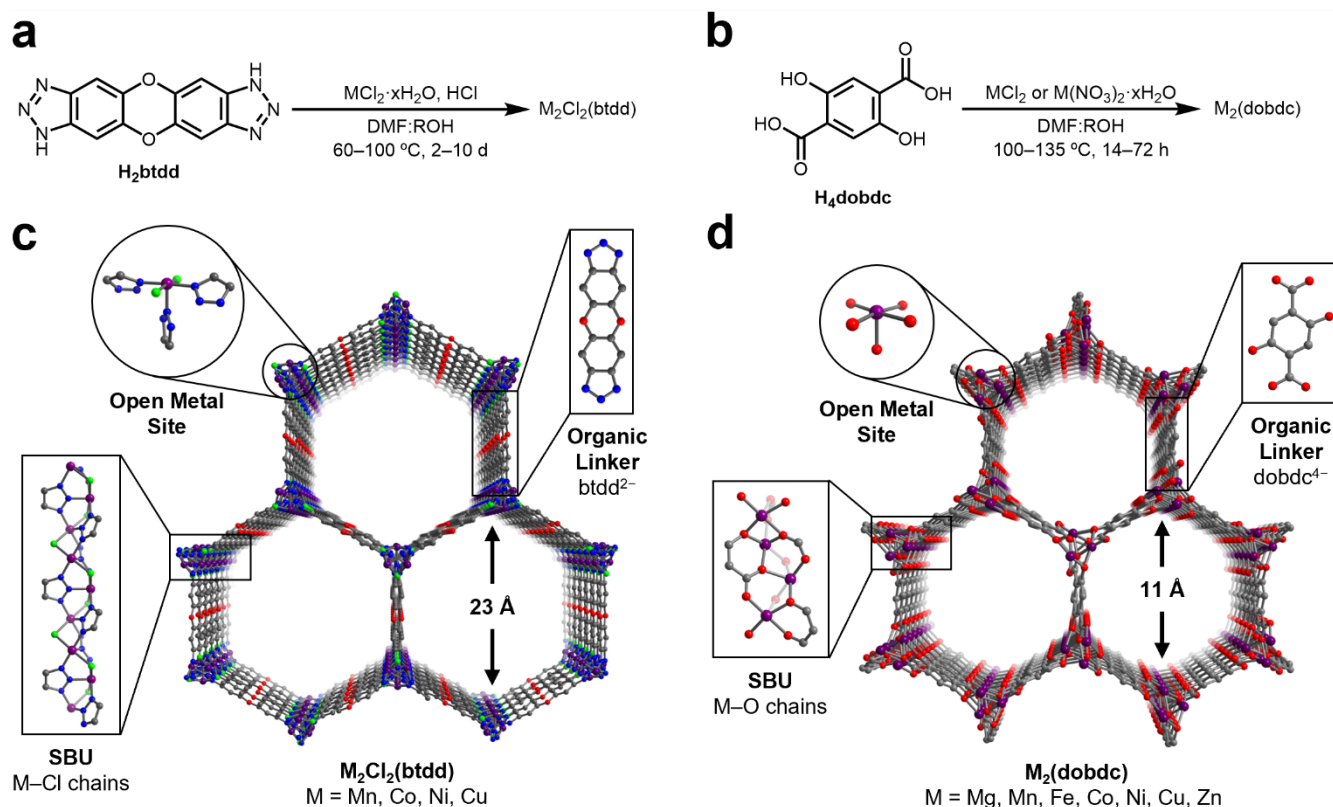**Figure 1.** General synthesis conditions of a) M_2Cl_2(btdd) (M = Mn, Co, Ni, Cu) and b) M_2(dobdc) (M = Mg, Mn, Fe, Co, Ni, Cu, Zn) MOFs (R = Et, Me, *i*Pr, H). Structures of c) M_2Cl_2(btdd) and d) M_2(dobdc). Purple, light green, blue, grey, and red spheres represent metal, chlorine, nitrogen, carbon, and oxygen atoms, respectively. Hydrogen atoms are omitted for clarity.

and more. In contrast, only a small number of largely unrelated MOFs have been studied for N_2O capture to date.[18–24] The presence of Lewis acidic open-metal-sites has been shown to enhance N_2O binding;[19] however, a general lack of structure-property trends informing the design of new materials hinders improvements in N_2O capture in porous materials.

Herein, we present a structure-activity study of N_2O adsorption in MOFs, with the purpose of identifying features that lead to strong binding and high uptake. Through a combined experimental and computational analysis, we clarify the effects of the ligand field and metal identity on N_2O adsorption at Lewis acidic open-metal-sites in the M_2Cl_2(btdd) (M= Mn, Co, Ni, Cu; btdd^{2-} = bis(1,2,3-triazolo[4,5-b],[4',5'-*i*])dibenzo[1,4]dioxin)[25–27] and M_2(dobdc) (M = Mg, Mn, Fe, Co, Ni, Cu, Zn; dobdc^{4-} = 2,5-dioxido-1,4-benzenedicarboxylate) series of MOFs.[12,28,29] From this analysis, we identify the M_2(dobdc) series, particularly Mg_2(dobdc) and Ni_2(dobdc), as promising adsorbents that display strong binding and record-setting N_2O adsorption capacities.

Beyond reducing its environmental impact, N_2O capture is incentivized by the opportunity to utilize it as a cheap, abundant, and potent oxidant in organic synthesis.[30–32] As a kinetically inert molecule, transition metal catalysts and/or high temperatures and pressures are required to facilitate N_2O activation. Thus, MOFs and zeolites containing Fe(II) sites have been explored as catalysts for N_2O functionalization.[33–38] In particular, Fe_2(dobdc) has been demonstrated to catalyze C–H oxidation of hydrocarbons using N_2O as an oxidant.[36,39–41]

Bearing strong similarities to enzymatic iron-based catalysts,[42–44] this occurs through a 2 e$^-$ transfer from high spin Fe(II) to the oxygen of N_2O, cleaving the N–O bond and forming a high spin Fe(IV)–oxo intermediate. This process is calculated to be followed by σ-attack and H atom abstraction by the Fe(IV)–oxo and radical rebound to generate the oxidized product.[39] Herein, DFT calculations support that N_2O activation is also thermodynamically favorable in Mn_2(dobdc), and we map out an approximate reaction coordinate for this process using the climbing-image nudged elastic band method (CI-NEB). While combined analysis of computation and experiment suggests that this reaction is kinetically limited in Mn_2(dobdc), our work motivates further study of N_2O activation in related Mn-based MOFs. Overall, our findings stimulate the development of new framework materials for selective N_2O capture and conversion to mitigate its environmentally destructive impact.

Results and Discussion

N_2O adsorption analysis.

N_2O is a weakly σ-donating and π-accepting ligand, which has limited the number of well-characterized transition metal adducts of N_2O to only a small handful, typically bound as η^1-N or η^2-N,N coordinated N_2O through π-backbonding interactions.[45–51] Although N_2O has a relatively weak dipole moment (0.161 D),[52] sorbents could compensate by incorporating Lewis acidic sites to strengthen electrostatic interactions between N_2O and the sorbent material. MOFs

containing highly Lewis acidic coordinatively unsaturated metal centers are effective adsorbents for a wide variety of gases through strong electrostatic interactions.[53] To identify robust structure-property trends regarding N_2O binding at open-metal-sites, we targeted isostructural frameworks accommodating a range of metal ions in similar ligand fields. These criteria should effectively yield insights into the interplay of the metal identity and ligand field on the binding strength of N_2O at open-metal-sites in MOFs.

Two groups of MOFs that fulfil these requirements are the $M_2Cl_2(btdd)$ and $M_2(dobdc)$ series. These MOFs are composed of hexagonal-pored structures formed by connecting one-dimensional, rod-like metal SBUs with ditopic organic linkers (Figure 1). Porous channels extend through the materials and, after activation, become lined with a high density of coordinatively unsaturated metal sites confined in square pyramidal geometries. While the overall structures of the $M_2Cl_2(btdd)$ and $M_2(dobdc)$ series are similar, their SBUs lead to distinctive ligation of the metal sites. In $M_2Cl_2(btdd)$, metal ions are coordinated to three individual triazolate groups through one nitrogen atom per triazolate. Each triazolate coordinates to three distinct metal ions, and two chlorides (μ_2) bridge neighboring metals, forming M–Cl chains. For this study, the isostructural Mn, Co, Ni, and Cu MOFs of this series were synthesized according to reported procedures (Figure 1a, SI sections 3–6).[25,27,54] In the $M_2(dobdc)$ series, the secondary building units are composed of metal-salicylate chains, forming an oxygen-based ligand field. The Mg, Mn, Fe, Co, Ni, Cu, and Zn variants of $M_2(dobdc)$ were synthesized in accordance with the literature (Figure 1b, SI sections 7–13).[12,29,55–58] All MOFs analyzed in this study were confirmed to be highly crystalline and match the expected structures via powder X-ray diffraction (PXRD). The porosity of all MOFs was confirmed using 77 K N_2 adsorption/desorption measurements. The calculated surface areas are similar to those reported in the literature in every case.

After synthesis, the MOFs were each evaluated as N_2O sorbents by measuring N_2O adsorption and desorption isotherms at 25 °C, 35 °C, and 45 °C (SI sections 3–13). Adsorption data were fit using dual-site Langmuir-Freundlich models (SI Eq S1). These fits were subsequently used to calculate enthalpies of N_2O adsorption ($-\Delta H_{ads}$) in each MOF using the Clausius-Clapeyron equation (SI Eq S2). The resulting $-\Delta H_{ads}$ values as a function of N_2O uptake in both series of MOFs are summarized in Figure 2 and Table 1. Critically, PXRD and surface area measurements confirm the stability of every MOF towards N_2O except for $Fe_2(dobdc)$, which has been previously shown to react irreversibly with this gas.[36,39–41] As a result, the adsorption data for this MOF were excluded from the analysis below.

The $M_2Cl_2(btdd)$ series were first evaluated as N_2O sorbents. Despite their high density of open-metal-sites, all MOFs of this series only weakly interact with N_2O ($-\Delta H_{ads} < 25$ kJ/mol). The difference in binding strength between the variants is minor: Co, Ni, and Mn analogues exhibit similar binding strengths, followed by Cu (Table 1). MOFs bearing coordinatively
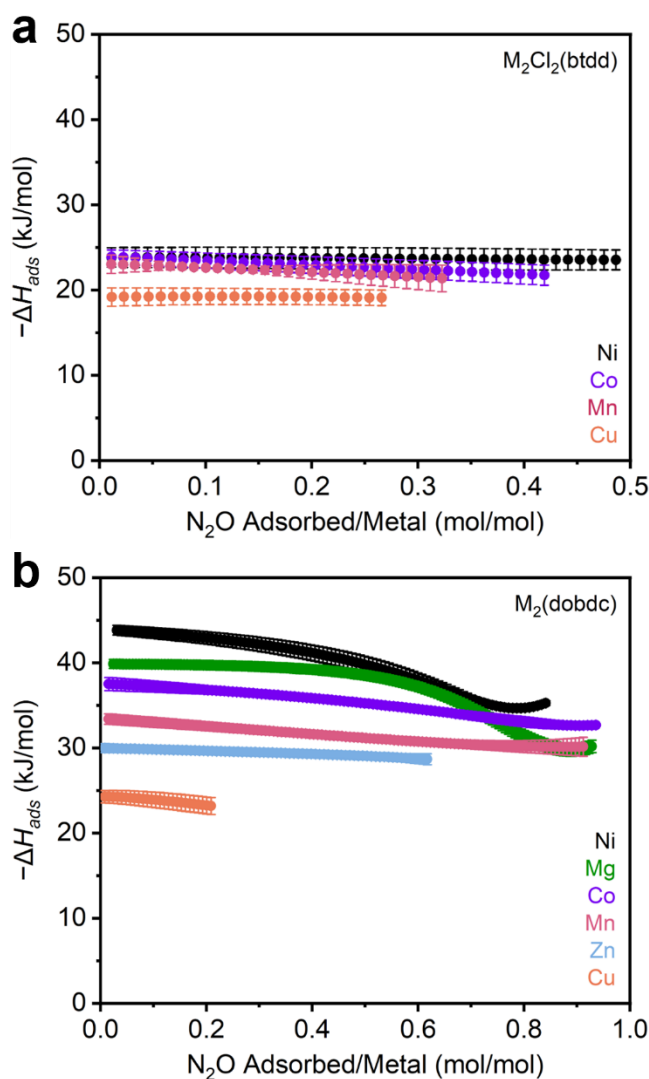

Figure 1. a)–ΔH_{ads} vs. N_2O uptake calculated from N_2O adsorption isotherms in a) $M_2Cl_2(btdd)$ (M = Ni, Co, Cu, Mn) and b) $M_2(dobdc)$ (M = Ni, Mg, Co, Mn, Zn, Cu) MOFs.

unsaturated Cu sites are commonly poor adsorbents due to Jahn-Teller axial distortion at the Cu sites.[12,59] Lacking substantial differences in binding strength between variants, the influence of the metal identity appears to be overshadowed by that of the ligand field in the $M_2Cl_2(btdd)$ series. The Lewis acidities of the metals are likely tempered by the electron-donating coordination environment of triazolate and chloride

Table 1 N_2O adsorption enthalpies and maximum uptake values at 298 K in $M_2Cl_2(btdd)$ and $M_2(dobdc)$ MOFs.

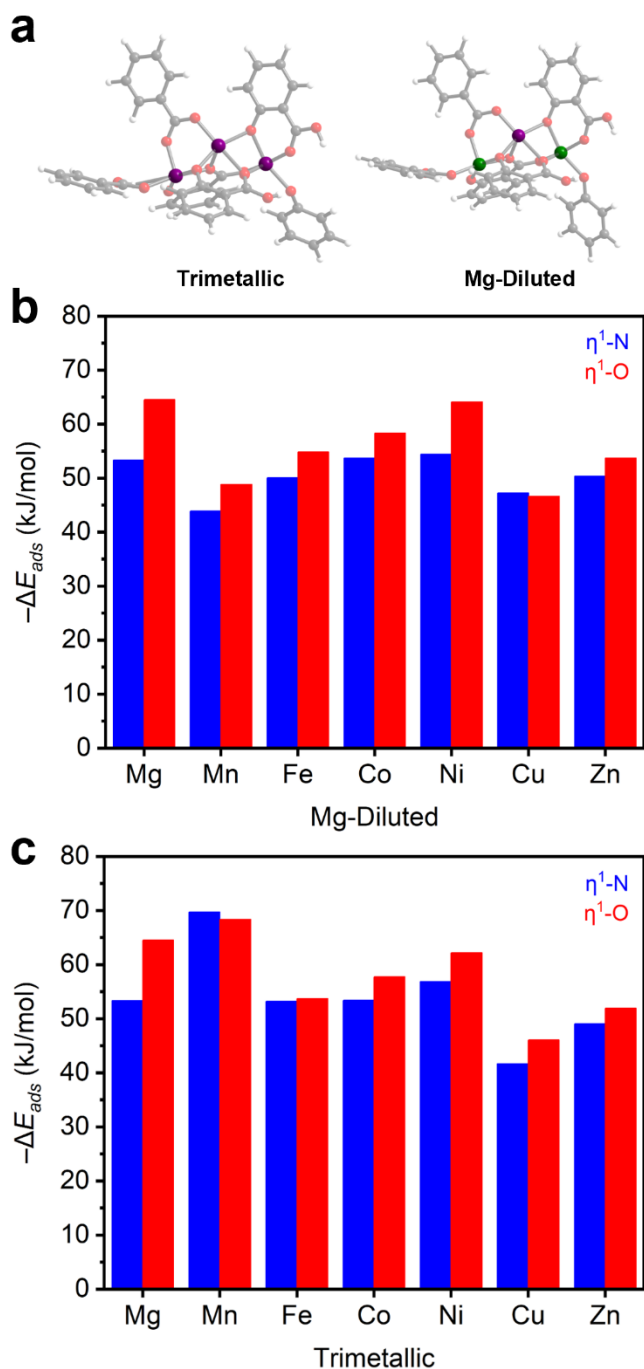| MOF	$-\Delta H_{ads}$ N_2O (kJ/mol)	Maximum Uptake at 298 K (mmol/g)
$Mn_2Cl_2(btdd)$	23.0 ± 1.1	2.37
$Co_2Cl_2(btdd)$	23.9 ± 0.8	3.10
$Ni_2Cl_2(btdd)$	23.8 ± 1.1	3.49
$Cu_2Cl_2(btdd)$	19.2 ± 1.1	1.86
$Mg_2(dobdc)$	39.9 ± 0.5	8.75
$Mn_2(dobdc)$	33.4 ± 0.6	7.77
$Co_2(dobdc)$	37.5 ± 0.8	7.26
$Ni_2(dobdc)$	43.8 ± 0.6	6.44
$Cu_2(dobdc)$	24.3 ± 0.7	2.21
$Zn_2(dobdc)$	30.0 ± 0.5	5.37

Figure 3. a) Trimetallic (left) and Mg-diluted (right) cluster models of M_2(dobdc). Purple, green, grey, red, and white spheres represent metal, magnesium, carbon, oxygen, and hydrogen atoms, respectively. DFT-calculated negative adsorption energies ($-\Delta E_{ads}$) of η^1-N (blue) and η^1-O (red) coordinated N_2O in the b) Mg-diluted and c) trimetallic systems.

Decreasing the ligand field strength surrounding the open-metal-sites should produce more Lewis acidic metal centers and thus lead to stronger electrostatic interactions with N_2O. Switching from M_2Cl_2(btdd) to M_2(dobdc) preserves the coordination geometry of the metal centers, but the oxygen-based SBU provides a weaker ligand field overall. Indeed, every member of the M_2(dobdc) series binds N_2O more strongly at low pressures than the M_2Cl_2(btdd) MOFs (Figure 2b). Moreover, the comparatively electron-deficient coordination environments in this series emphasize the influence of the metal identity on N_2O binding strengths; enthalpies of adsorption vary by as much as 20 kJ/mol among M_2(dobdc) variants (Table 1). N_2O binding strengths in these series mirror the empirical Irving-Williams series: Cu < Zn < Mn < Co < Mg < Ni.[60] Like Cu_2Cl_2(btdd), Cu_2(dobdc) likely exhibits weak N_2O adsorption because of axial distortion.[12] In contrast, Mg_2(dobdc) is an especially effective N_2O adsorbent due to the hard nature of its Lewis acidic Mg(II) cations. As the effective charge of the transition metal centers increases from Mn to Ni,[61] the N_2O binding strengths increase as well. As a result, Ni_2(dobdc) is the strongest N_2O adsorbent assessed in this study ($-\Delta H_{ads}$ = 43.8 ± 0.6 kJ/mol). Compared to other commonly studied gases (CO_2, O_2, N_2), N_2O is generally more strongly bound by the M_2(dobdc) series, which is likely due to its modest dipole moment. In particular, N_2O binding is approximately 2–6 kJ/mol stronger than CO_2 in all cases except for in Mg_2(dobdc), in which CO_2 binds more strongly by approximately 3 kJ/mol.[12] O_2 and N_2 binding enthalpies are consistently 10–20 kJ lower than those of N_2O as well.[62] These findings highlight the discrepancy between the comparatively strong binding of N_2O at metal centers compared to CO_2, O_2, and N_2 and the lack of well-characterized N_2O-bound metal complexes.[45–49]

Strong N_2O binding is accompanied by relatively high N_2O capacities in the M_2(dobdc) series of frameworks. In particular, the second-strongest adsorbent of N_2O identified in this work, Mg_2(dobdc), adsorbs 8.75 mmol/g at 1000 mbar of N_2O and 298 K, surpassing the previous record-holder, MIL-100 (Cr) (5.78 mmol/g, MIL = Materials Institute Lavoisier), by a significant margin.[20] The Mn, Co, and Ni M_2(dobdc) variants also exceed the previous record for N_2O uptake in a MOF. Overall, this comparison underlines the M_2(dobdc) series, especially Mg_2(dobdc), as promising adsorbents that exhibit high gravimetric N_2O capacities coupled with strong and tuneable binding strengths.

Computational survey of N_2O adsorption.

After establishing the M_2(dobdc) series as effective N_2O adsorbents, we further evaluated N_2O binding in this series using DFT calculations (SI section 14). For these calculations, trimetallic cluster models were generated to approximately study the one-dimensional chain SBU (Figure 3a). Similar cluster models have been used to evaluate N_2O reduction in Fe_2(dobdc).[39,40] For each member of the M_2(dobdc) series, excluding Mg_2(dobdc) for redundancy, two types of cluster models were simulated: a trimetallic system and a Mg-diluted system. In the Mg-diluted models, both edge metal ions were replaced with Mg(II) ions. The purpose of including the Mg-

ligands. These ligands produce electron-rich metal centers that are less Lewis acidic than those found in other materials. Although these MOFs are capable of binding polar gases such as NH_3,[25] the absence of a significant dipole moment on N_2O makes the M_2Cl_2(btdd) MOFs ineffective N_2O adsorbents. Lacking suitable binding sites, the M_2Cl_2(btdd) series show very limited uptakes; the quantity of N_2O adsorbed under equilibrium conditions, even at 1000 mbar N_2O and 298 K (Table 1), does not come close to saturating the available open-metal-sites.

diluted systems is to simulate only one open-shell metal center and decouple adsorption energetics from the potential influence of metal-metal coupling on N_2O adsorption. All systems are neutral with all M(II) ions in the high-spin state where applicable (SI Table S13).

The energies of adsorption ($-\Delta E_{ads}$) for both η^1-N and η^1-O coordinated N_2O adducts in the model clusters were first calculated (Figure 3b–c, SI Table S11). In both the trimetallic and Mg-diluted models, η^1-O coordinated N_2O is slightly more stabilized (2–10 kJ/mol) than η^1-N coordinated N_2O. This aligns with the approximately 60%/40% η^1-O/η^1-N population split determined from neutron diffraction data collected on N_2O-dosed $Fe_2(dobdc)$.[36] The calculated formation energies of N_2O adducts in the Mg-diluted series (Figure 3b) approximately match the trend observed experimentally: Cu ≈ Mn < Fe ≈ Zn < Co < Ni ≈ Mg. However, some divergence is noted in the trimetallic systems (Figure 3c): the Mn-based trimetallic system binds N_2O considerably more strongly than the equivalent Mg-diluted model, suggesting multiple metal effects that require consideration of metal-metal coupling (see below). Additionally, η^1-N coordination to $Mn_2(dobdc)$ is slightly more favorable than η^1-O in the trimetallic model.

Across the series, the model systems reveal that η^1-O and η^1-N adducts of N_2O are bent, with bond angles and M–N_2O distances in agreement with those solved from the neutron diffraction data in N_2O–$Fe_2(dobdc)$ (SI Table S12), the only definitively characterized structure of N_2O bound to a metal center within a MOF reported to date.[36] In the DFT-calculated structure, η^1-N coordinated N_2O exhibits a typical bond angle of 115–123° (122° in N_2O–$Fe_2(dobdc)$), whereas η^1-O coordinated N_2O exhibits slightly smaller bond angles ranging from 105–120° (117° in N_2O–$Fe_2(dobdc)$). Bond lengths of η^1-N and η^1-O coordinated N_2O (2.25–2.57 Å and 2.27–2.54 Å, respectively) vary over only a narrow range. These models reinforce that N_2O binding across the $M_2(dobdc)$ series is primarily based on electrostatic interactions rather than π-backbonding, which would be expected to lead to linear η^1-N (V, Cu, Ru, Rh) or side-on η^2-N,N (Co, Ni) interactions with N_2O.[45–51]

It should be noted that N_2O adsorption has been modelled previously in a small variety of other open-metal-site MOFs. The Fe(II)- and Cu(II)-based paddlewheel nodes in $M_3(btc)_2$ (btc^{3-} = benzene-1,3,5-tricarboxylate) MOFs show bent η^1-N and η^1-O coordination modes for N_2O.[53] Likewise, N_2O adducts have been modelled for the trinuclear carboxylate-bridged, oxygen-centered nodes ($M_3(\mu_3$-O)(RCOO)$_6$, M = V, Cr, Mn, Fe, Co, Ni) common among MOFs such as MIL-100, MIL-101, and MIL-127.[63] The calculated binding of η^1-N coordinated N_2O at V centers is linear, but other adducts are bent, with similar bond angles and bond lengths as calculated in the $M_2(dobdc)$ series herein. In the Kuratowski-type SBU of Cu-MFU-4*l* (MFU = Metal-Organic Framework Ulm-University), DFT calculations support an approximately linear η^1-N coordinated N_2O molecule, indicating possible π-backbonding from the Cu(I) centers.[19] Overall, these findings support that N_2O is predicted to bind in a bent fashion at most metal centers in MOFs.

A notable exception to the trends outlined above is the trimetallic Mn cluster, in which η^1-N coordinated N_2O is nearly linear (172°), suggesting that π-backbonding occurs from the Mn *d* orbitals into the π* orbital of N_2O, which has previously been invoked in linear η^1-N V, Cu, Ru, and Rh adducts of N_2O to justify the unusual stability of those complexes.[45,47–49,51] Consistently, the Mn–N bond length (1.95 Å) is considerably shorter than in other models (SI Figure S68). These characteristics are distinct from the equivalent Mg-diluted cluster, suggesting that metal-metal coupling may affect the binding mode of N_2O in these calculations. We thus evaluated N_2O binding in the open-shell trimetallic systems (Mn through Cu) using broken-symmetry density functional theory (BS-DFT) with two spin flip configurations (i.e., in the central metal or in one edge metal) to quantify the metal-metal coupling and to extract coupling constants (SI Figure S69, SI section 14). To ensure that the BS-DFT calculations converged to the desired states, the spin density was visually inspected (SI Figure S70). In particular, the energetic difference in the trimetallic Mn system in comparison to the dilute case indicates especially strong metal-metal coupling (SI Table S14). From this data, we calculated strong magnetic coupling along the SBU chains in the trimetallic Mn system (J = 314.27 cm^{-1}), which becomes even stronger after N_2O binding regardless of the coordination mode (J = 857.47 cm^{-1} for η^1-N, J = 857.47 cm^{-1} for η^1-O). Consistently, magnetic susceptibility measurements (SI Figure S77) and prior first principles studies support that $Mn_2(dobdc)$ exhibits antiferromagnetic coupling below approximately 27 K.[61,64] Adsorbate-induced changes in magnetic coupling are also precedented in the $M_2(dobdc)$ series; for example, in $Fe_2(dobdc)$, the ferromagnetic exchange strength along the SBU chains is attenuated by interaction with weak adsorbates (e.g., CH_4, $-\Delta H_{ads}$ = 20 kJ/mol), and the coupling becomes antiferromagnetic upon interaction with strong adsorbates (e.g., C_2H_2, $-\Delta H_{ads}$ = 47 kJ/mol).[65] Our results point to an additional stabilization of the N_2O adducts of $Mn_2(dobdc)$ related to enhanced metal coupling, possibly leading to greater π-backbonding from Mn to N_2O and favoring linear η^1-N coordination. Above 27 K, however, this effect is no longer expected to significantly contribute to the adsorption interactions as the spins become randomly oriented. Consistently, the experimental binding enthalpies do not show enhanced adsorption in $Mn_2(dobdc)$ relative to other MOFs in the series. Nevertheless, if a suitable Mn-based open-metal-site MOF with a higher Neel temperature were to be identified, this feature could potentially be leveraged to enhance N_2O binding.

Evaluating N_2O activation in the $M_2(dobdc)$ series.

N_2O activation to form M(IV)-oxo species and N_2 in MOFs has been principally studied in $Fe_2(dobdc)$ and other Fe(II)-based frameworks.[36–40,66,67] Unfortunately, Fe(II)-based systems are prohibitively air sensitive for practical applications. Identifying more air-stable materials capable of N_2O activation would be a significant step towards utilizing N_2O as a green oxidant. In order to determine whether this reactivity is unique to $Fe_2(dobdc)$, the same cluster models were used to calculate the favorability of M(IV)-oxo formation in the remainder of the $M_2(dobdc)$ series (SI Table S15, SI section 14). DFT calculations with both the trimetallic and Mg-diluted cluster model series

show that, in addition to Fe$_2$(dobdc), M(IV)-oxo formation is thermodynamically favorable ($\Delta E_f < 0$ kJ/mol) in Mn$_2$(dobdc) (Figure 4a, SI section 14). Indeed, M(IV)-oxo formation is calculated to be significantly more thermodynamically favorable in Mn$_2$(dobdc) (−183.1 and −176.1 kJ/mol for trimetallic and Mg-diluted systems, respectively) than in Fe$_2$(dobdc) (−55.5 and −52.7 kJ/mol for trimetallic and Mg-diluted systems, respectively). In contrast, M(IV)–oxo formation is endothermic in the Mg, Co, Ni, Cu, and Zn analogues, ruling out these materials as potential catalysts for N$_2$O activation. This is fairly expected due to the electronic instability of terminal M(IV)–oxo complexes of octahedral symmetry possessing greater than 5 d electrons.[68] Precedent for N$_2$O activation in Mn-based systems is found in manganese oxides, which catalyze the decomposition of N$_2$O[69] and the oxidation of 1-butene at high temperatures.[70] Likewise, Mn-substituted polyoxometalates have been shown to activate N$_2$O and catalyze the epoxidation of alkenes,[71,72] and Mn-substituted zeolites catalyze N$_2$O decomposition as well.[73,74]

To determine the potential viability of N$_2$O activation by Mn$_2$(dobdc), an approximate reaction coordinate for this process was modelled using the CI-NEB method (Figure 4b, Text S1). The η^1-O coordinated N$_2$O adduct of the Mg-diluted Mn$_2$(dobdc) cluster model was used as the initial state, and the Mn(IV)–oxo-containing Mg-diluted cluster was used as the final state (SI section 14). During N$_2$O activation, the Mn(IV)–oxo bond is formed and the O–N bond is broken, forming N$_2$. From the initial state, the M–O bond length shrinks significantly and is matched by a substantial lengthening of the O–N bond. During this transition, the energy of the system rises sharply early on, after which it falls to roughly the energy of the final state. Likewise, a constant M–O bond length, consistent with Mn(IV)–oxo formation, was observed in the second half of the reaction coordinate, as the rest of the pathway is characterized by O–N bond elongation as unbound N$_2$ moves away from the cluster. The approximate transition state of the reaction is rather early, with Mn–O and N–O bond lengths of 2.00 Å and 1.39 Å, respectively (Figure 4c). From the difference in energy between the initial state and this approximate transition state, the kinetic barrier to N$_2$O activation in this model cluster was calculated to be approximately 113 kJ/mol. This barrier is comparable to the calculated activation barriers of 167 kJ/mol in the Mn-based trinuclear MOF nodes and 109 kJ/mol in the Mn-substituted polyoxometalate discussed above.[63,72]

In previous studies, heating N$_2$O-dosed Fe$_2$(dobdc) at only 35 °C was sufficient to partially oxidize the material, and its complete oxidation was accomplished at 60 °C after prolonged heating.[36] The activation barrier for Fe(IV)–oxo formation in N$_2$O-bound Fe$_2$(dobdc) was calculated to be 94 kJ/mol (enthalpy of activation = 82 kJ/mol).[39] Although the calculated activation barrier for Mn(IV)–oxo formation in Mn$_2$(dobdc) is notably larger, the conditions that lead to Fe(IV)–oxo formation in Fe$_2$(dobdc) are mild. As such, we evaluated whether more forceful conditions (i.e., higher temperatures) could enable Mn(IV)–oxo formation in Mn$_2$(dobdc). To probe this possibility, N$_2$O adsorption measurements in Mn$_2$(dobdc) at 180 °C, 250 °C, and 300 °C were collected to identify potential N$_2$O activation

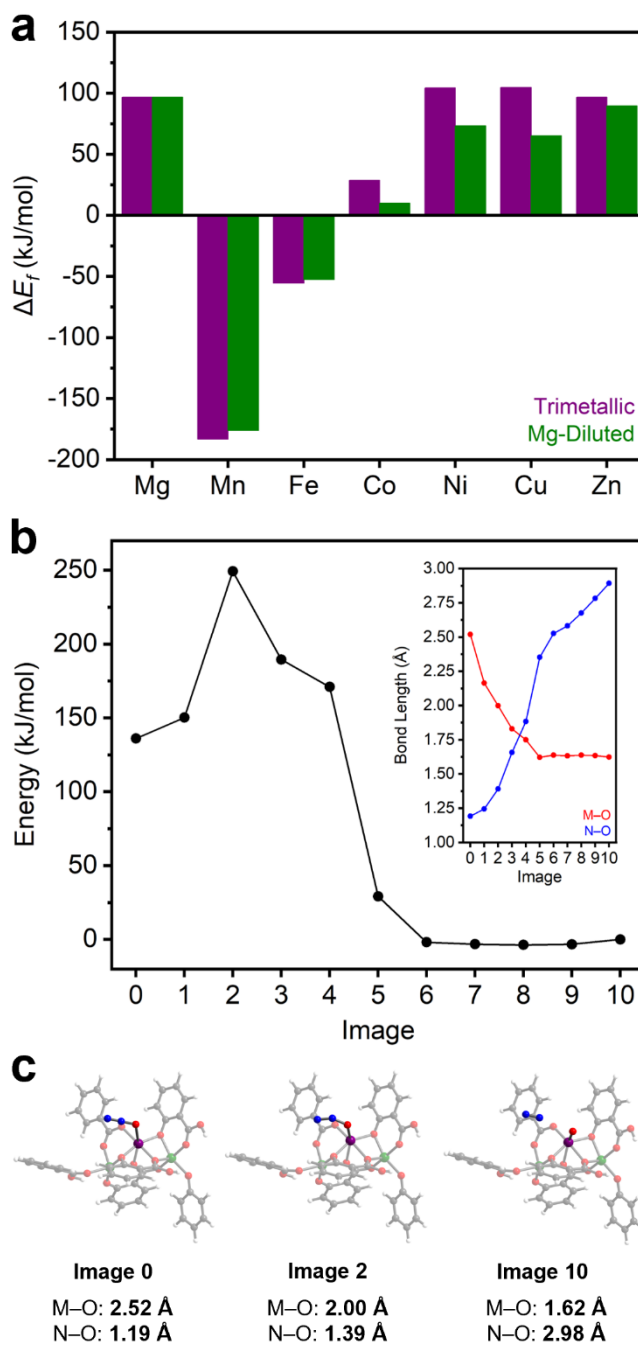**Figure 4.** a) DFT-calculated energies of M–oxo formation (ΔE_f) in the trimetallic (purple) and Mg-diluted (green) models of M$_2$(dobdc). b) CI-NEB-calculated approximate reaction coordinate of Mn–oxo formation from η^1-O coordinated N$_2$O in the Mg-diluted system. Inset: M–O (red) and N–O (blue) bond lengths vs. image number. c) Structures of the initial (left), transition (center), and final (right) states. Purple, green, blue, grey, red, and white spheres represent manganese, magnesium, nitrogen, carbon, oxygen, and hydrogen atoms, respectively.

through changes in the adsorption properties of the material (SI Figure S72). Fully reversible N$_2$O adsorption was measured at 180 °C; however, measurements at 250 °C and 300 °C consistently yielded anomalous negative adsorption, possibly indicating reactivity with the MOF. For further analysis, a bulk sample of Mn$_2$(dobdc) was prepared by dosing the MOF with N$_2$O at 300 °C (SI section 15). The BET surface area of Mn$_2$(dobdc) after heating at 300 °C (1285 ± 3 m^2/g) under vacuum for 24 h is comparable to that of the pristine MOF (1344 ± 3 m^2/g), supporting that this MOF is stable at elevated
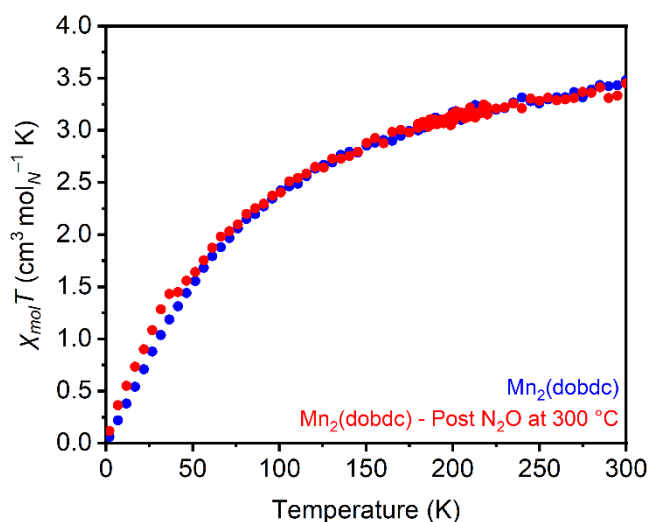
Figure 5. Variable-temperature magnetic susceptibility ($\chi_{mol}T$) measurements of Mn$_2$(dobdc) under an applied field of 1000 Oe before (blue) and after (red) N$_2$O treatment at 300 °C. The minor increase in $\chi_{mol}T$ of the N$_2$O-treated sample from approximately 2–40 K is attributed to slight O$_2$ contamination.

temperatures. Notably, the BET surface area is significantly attenuated after N$_2$O dosing at 300 °C (896 ± 2 m^2/g) (SI Figure S73). The reduction in surface area is accompanied by a color change from orange to brown. PXRD measurements confirm that Mn$_2$(dobdc) retains its crystallinity after this process, although some peak-broadening was observed, indicative of partial decomposition (SI Figure S74).

Magnetic susceptibility measurements were used to characterize the product(s) resulting from high-temperature treatment of Mn$_2$(dobdc) with N$_2$O. The magnetic moments in Mn$_2$(dobdc) calculated from susceptibility measurements before (μ_{eff} = 5.94 μ_B) and after (μ_{eff} = 5.89 μ_B) (Figures S80–81) N$_2$O treatment at 300 °C closely match the value expected for Mn(II) with a spin of 5/2 (5.92 μ_B), indicating a lack of oxidation at the metal center after N$_2$O treatment (Figure 5). Despite this, increased magnetic susceptibility relative to unreacted Mn$_2$(dobdc) was consistently noted in moment vs. field measurements collected at 5 K after N$_2$O treatment at 300 °C (SI Figure S82). This finding may point to reactivity between N$_2$O and the redox-active linker instead,[75] as oxidation of the high-spin Mn(II) sites to Mn(IV) should result in a decrease in the magnetic susceptibility.

To further characterize the reaction of Mn$_2$(dobdc) with N$_2$O, we utilized variable-temperature diffuse reflectance Fourier transform (DRIFTS) spectroscopy (SI Figures S75–76). A sample of Mn$_2$(dobdc) was heated under an atmosphere of N$_2$O (approx. 1 bar) from 25 °C to 300 °C and held at 300 °C for 15 h. Spectra were collected periodically throughout the duration of the measurement. New Mn–O stretches corresponding to Mn(IV)–oxo (approx. 845 cm^{-1})[76] or Mn(III)–OH species (600–700 cm^{-1})[77] were not observed (SI Figure S76). Likewise, stretches corresponding to quinone formation due to linker oxidation were not observed (1657 cm^{-1}).[75] However, a weak O–H stretching frequency at 3673 cm^{-1} emerged over time, and the prominent stretch at 1406 cm^{-1} reduced in intensity after prolonged treatment with N$_2$O (SI Figure S75). Overall, while the MOF appears to react with N$_2$O at high temperatures, the DRIFTS and magnetic data indicate a lack of oxidation at the

metal centers. This finding suggests that the high kinetic barrier to Mn(IV)–oxo formation in Mn$_2$(dobdc) is likely prohibitive, despite its thermodynamic favorability. Elucidating the products of this MOF's reaction with N$_2$O is the focus of ongoing work.

Conclusions

Herein, we identify features that contribute to strong binding and high uptake of N$_2$O at Lewis acidic, coordinatively unsaturated metal sites in MOFs. We utilize the M$_2$Cl$_2$(btdd) and M$_2$(dobdc) series as model systems to facilitate comparisons, as their general structures are related but distinguished by the ligation of the open-metal-sites. In the M$_2$Cl$_2$(btdd) series, the binding enthalpies of N$_2$O are generally low (<25 kJ/mol) and within error, despite variations in the metal identity. In contrast, the salicylate-based SBU in the M$_2$(dobdc) series provides a weaker, oxygen-based ligand field. N$_2$O binding strengths in these MOFs mostly mirror the Irving-Williams series, with Ni$_2$(dobdc) exhibiting the strongest adsorption of N$_2$O among all tested MOFs ($-\Delta H_{ads}$ = 43.8 ± 0.6). Notably, Mg$_2$(dobdc) exhibits a record-breaking N$_2$O gravimetric capacity (8.75 mmol/g at 1000 mbar of N$_2$O and 298 K) among MOFs. While these Lewis acidic sites are effective for N$_2$O capture, they are not necessarily selective for N$_2$O among other polar(izable) gases, such as H$_2$O.[78] Achieving selective adsorption of N$_2$O at open-metal-sites will be the focus of future work.

Using the cluster systems to computationally model the oxidation of the M$_2$(dobdc) series by N$_2$O, forming M(IV)–oxo species, we find that M–oxo formation is also thermodynamically favorable in Mn$_2$(dobdc) according to DFT calculations. We thus used the CI-NEB method to map a reaction coordinate for this process and determined an approximate activation barrier of 113 kJ/mol, which is higher than that calculated for Fe$_2$(dobdc) (94 kJ/mol). Although experiments indicate that this kinetic barrier is too high to be overcome in Mn$_2$(dobdc), these findings suggest that Mn-based MOFs may be promising alternatives to traditionally studied Fe-based materials for N$_2$O activation.

Overall, this work adds to the growing body of research seeking to utilize N$_2$O as a green oxidant, in which Mn-based solid-state catalysts remain relatively understudied. The results reported herein will help to drive the identification and development of other effective MOF-based sorbents to mitigate environmentally destructive N$_2$O emissions.

Author Contributions

P.J.M and H.J.K. conceived the project. T.A.P. carried out the synthesis, characterization, and gas sorption measurements of MOF samples under the supervision of P.J.M. P.J.M. and M.E.Z. also synthesized MOF samples. H.J. and A.N. carried out computational studies under the supervision of H.J.K. T.J.A. carried out magnetic measurements. T.A.P. and H.J. prepared the first draft of the manuscript, which was edited and approved by all co-authors.

Conflicts of Interest

Acknowledgements

Notes and References

1   Davidson, E. A.; Winiwarter, W. Urgent Abatement of Industrial Sources of Nitrous Oxide. *Nat. Clim. Chang.* **2023**, *13* (7), 599–601. https://doi.org/10.1038/s41558-023-01723-3.

2   Intergovernmental Panel On Climate Change. *Climate Change 2021 – The Physical Science Basis: Working Group I Contribution to the Sixth Assessment Report of the Intergovernmental Panel on Climate Change*, 1st ed.; Cambridge University Press, 2023. https://doi.org/10.1017/9781009157896.

3   Tian, H.; Xu, R.; Canadell, J. G.; Thompson, R. L.; Winiwarter, W.; Suntharalingam, P.; Davidson, E. A.; Ciais, P.; Jackson, R. B.; Janssens-Maenhout, G.; Prather, M. J.; Regnier, P.; Pan, N.; Pan, S.; Peters, G. P.; Shi, H.; Tubiello, F. N.; Zaehle, S.; Zhou, F.; Arneth, A.; Battaglia, G.; Berthet, S.; Bopp, L.; Bouwman, A. F.; Buitenhuis, E. T.; Chang, J.; Chipperfield, M. P.; Dangal, S. R. S.; Dlugokencky, E.; Elkins, J. W.; Eyre, B. D.; Fu, B.; Hall, B.; Ito, A.; Joos, F.; Krummel, P. B.; Landolfi, A.; Laruelle, G. G.; Lauerwald, R.; Li, W.; Lienert, S.; Maavara, T.; MacLeod, M.; Millet, D. B.; Olin, S.; Patra, P. K.; Prinn, R. G.; Raymond, P. A.; Ruiz, D. J.; Van Der Werf, G. R.; Vuichard, N.; Wang, J.; Weiss, R. F.; Wells, K. C.; Wilson, C.; Yang, J.; Yao, Y. A Comprehensive Quantification of Global Nitrous Oxide Sources and Sinks. *Nature* **2020**, *586* (7828), 248–256. https://doi.org/10.1038/s41586-020-2780-0.

4   Ravishankara, A. R.; Daniel, J. S.; Portmann, R. W. Nitrous Oxide (N₂O): The Dominant Ozone-Depleting Substance Emitted in the 21st Century. *Science* **2009**, *326* (5949), 123–125. https://doi.org/10.1126/science.1176985.

5   Hassan, M. U.; Aamer, M.; Mahmood, A.; Awan, M. I.; Barbanti, L.; Seleiman, M. F.; Bakhsh, G.; Alkharabsheh, H. M.; Babur, E.; Shao, J.; Rasheed, A.; Huang, G. Management Strategies to Mitigate N₂O Emissions in Agriculture. *Life* **2022**, *12* (3), 439. https://doi.org/10.3390/life12030439.

6   Gu, B.; Zhang, X.; Lam, S. K.; Yu, Y.; Van Grinsven, H. J. M.; Zhang, S.; Wang, X.; Bodirsky, B. L.; Wang, S.; Duan, J.; Ren, C.; Bouwman, L.; De Vries, W.; Xu, J.; Sutton, M. A.; Chen, D. Cost-Effective Mitigation of Nitrogen Pollution from Global Croplands. *Nature* **2023**, *613* (7942), 77–84. https://doi.org/10.1038/s41586-022-05481-8.

7   Li, L.; Xu, J.; Hu, J.; Han, J. Reducing Nitrous Oxide Emissions to Mitigate Climate Change and Protect the Ozone Layer. *Environ. Sci. Technol.* **2014**, *48* (9), 5290–5297. https://doi.org/10.1021/es404728s.

8   Ding, M.; Flaig, R. W.; Jiang, H.-L.; Yaghi, O. M. Carbon Capture and Conversion Using Metal–Organic Frameworks and MOF-Based Materials. *Chem. Soc. Rev.* **2019**, *48* (10), 2783–2828. https://doi.org/10.1039/C8CS00829A.

9   Firooz, S. K.; Armstrong, D. W. Metal-Organic Frameworks in Separations: A Review. *Analytica Chimica Acta* **2022**, *1234*, 340208. https://doi.org/10.1016/j.aca.2022.340208.

10   Bavykina, A.; Kolobov, N.; Khan, I. S.; Bau, J. A.; Ramirez, A.; Gascon, J. Metal–Organic Frameworks in Heterogeneous Catalysis: Recent Progress, New Trends, and Future Perspectives. *Chem. Rev.* **2020**, *120* (16), 8468–8535. https://doi.org/10.1021/acs.chemrev.9b00685.

11   Furukawa, H.; Cordova, K. E.; O'Keeffe, M.; Yaghi, O. M. The Chemistry and Applications of Metal-Organic Frameworks. *Science* **2013**, *341* (6149), 1230444. https://doi.org/10.1126/science.1230444.

12   Queen, W. L.; Hudson, M. R.; Bloch, E. D.; Mason, J. A.; Gonzalez, M. I.; Lee, J. S.; Gygi, D.; Howe, J. D.; Lee, K.; Darwish, T. A.; James, M.; Peterson, V. K.; Teat, S. J.; Smit, B.; Neaton, J. B.; Long, J. R.; Brown, C. M. Comprehensive Study of Carbon Dioxide Adsorption in the Metal–Organic Frameworks M₂(dobdc) (M = Mg, Mn, Fe, Co, Ni, Cu, Zn). *Chem. Sci.* **2014**, *5* (12), 4569–4581. https://doi.org/10.1039/C4SC02064B.

13   He, Y.; Zhou, W.; Qian, G.; Chen, B. Methane Storage in Metal–Organic Frameworks. *Chem. Soc. Rev.* **2014**, *43* (16), 5657–5678. https://doi.org/10.1039/C4CS00032C.

14   Lin, Y.; Kong, C.; Chen, L. Amine-Functionalized Metal–Organic Frameworks: Structure, Synthesis and Applications. *RSC Adv.* **2016**, *6* (39), 32598–32614. https://doi.org/10.1039/C6RA01536K.

15   Sharifzadeh, Z.; Morsali, A. Amine-Functionalized Metal-Organic Frameworks: From Synthetic Design to Scrutiny in Application. *Coord. Chem. Rev.* **2022**, *459*, 214445. https://doi.org/10.1016/j.ccr.2022.214445.

16   Zick, M. E.; Cho, D.; Ling, J.; Milner, P. J. Carbon Capture Beyond Amines: CO₂ Sorption at Nucleophilic Oxygen Sites in Materials. *ChemNanoMat* **2023**, *9* (1), e202200436. https://doi.org/10.1002/cnma.202200436.

17   Li, J.; Han, X.; Zhang, X.; Sheveleva, A. M.; Cheng, Y.; Tuna, F.; McInnes, E. J. L.; McCormick McPherson, L. J.; Teat, S. J.; Daemen, L. L.; Ramirez-Cuesta, A. J.; Schröder, M.; Yang, S. Capture of Nitrogen Dioxide and Conversion to Nitric Acid in a Porous Metal–Organic Framework. *Nat. Chem.* **2019**, *11* (12), 1085–1090. https://doi.org/10.1038/s41557-019-0356-0.

18   Zhang, X.; Chen, W.; Shi, W.; Cheng, P. Highly Selective Sorption of CO₂ and N₂O and Strong Gas-Framework Interactions in a Nickel(II) Organic Material. *J. Mater. Chem. A* **2016**, *4* (41), 16198–16204. https://doi.org/10.1039/C6TA06572D.

19   Denysenko, D.; Jelic, J.; Magdysyuk, O. V.; Reuter, K.; Volkmer, D. Elucidating Lewis Acidity of Metal Sites in MFU-4*l* Metal-Organic Frameworks: N₂O and CO₂ Adsorption in MFU-4*l*, CuI-MFU-4*l* and Li-MFU-4*l*. *Microporous and Mesoporous Materials* **2015**, *216*, 146–150. https://doi.org/10.1016/j.micromeso.2015.03.014.

20   Yang, J.; Du, B.; Liu, J.; Krishna, R.; Zhang, F.; Zhou, W.; Wang, Y.; Li, J.; Chen, B. MIL-100Cr with Open Cr Sites for a Record

N2O Capture. *Chem. Commun.* **2018**, *54* (100), 14061–14064. https://doi.org/10.1039/C8CC07679K.

21 Ma, L.; Zhang, F.; Li, K.; Zhang, Y.; Song, Z.; Wang, L.; Yang, J.; Li, J. Improved N2O Capture Performance of Chromium Terephthalate MIL-101 via Substituent Engineering. *J. Solid State Chem.* **2022**, *309*, 122951. https://doi.org/10.1016/j.jssc.2022.122951.

22 Wang, L.; Zhang, F.; Yang, J.; Li, L.; Li, J. The Efficient Separation of N2O/CO2 Using Unsaturated Fe^{2+} Sites in MIL-100Fe. *Chem. Commun.* **2021**, *57* (54), 6636–6639. https://doi.org/10.1039/D1CC01659H.

23 Saha, D.; Bao, Z.; Jia, F.; Deng, S. Adsorption of CO2, CH4, N2O, and N2 on MOF-5, MOF-177, and Zeolite 5A. *Environ. Sci. Technol.* **2010**, *44* (5), 1820–1826. https://doi.org/10.1021/es9032309.

24 Wang, L.; Li, Y.; Wang, Y.; Yang, J.; Li, L.; Li, J. Research on CO2-N2O Separation Using Flexible Metal Organic Frameworks. *Sep. Purif. Technol.* **2020**, *251*, 117311. https://doi.org/10.1016/j.seppur.2020.117311.

25 Rieth, A. J.; Tulchinsky, Y.; Dincă, M. High and Reversible Ammonia Uptake in Mesoporous Azolate Metal–Organic Frameworks with Open Mn, Co, and Ni Sites. *J. Am. Chem. Soc.* **2016**, *138* (30), 9401–9404. https://doi.org/10.1021/jacs.6b05723.

26 Azbell, T. J.; Pitt, T. A.; Bollmeyer, M. M.; Cong, C.; Lancaster, K. M.; Milner, P. J. Ionothermal Synthesis of Metal-Organic Frameworks Using Low-Melting Metal Salt Precursors. *Angew. Chem. Int. Ed.* **2023**, *62* (17), e2022182. https://doi.org/10.1002/anie.202218252.

27 Park, S. S.; Tulchinsky, Y.; Dincă, M. Single-Ion Li$^+$, Na$^+$, and Mg^{2+} Solid Electrolytes Supported by a Mesoporous Anionic Cu–Azolate Metal–Organic Framework. *J. Am. Chem. Soc.* **2017**, *139* (38), 13260–13263. https://doi.org/10.1021/jacs.7b06197.

28 Caskey, S. R.; Wong-Foy, A. G.; Matzger, A. J. Dramatic Tuning of Carbon Dioxide Uptake via Metal Substitution in a Coordination Polymer with Cylindrical Pores. *J. Am. Chem. Soc.* **2008**, *130* (33), 10870–10871. https://doi.org/10.1021/ja8036096.

29 Bloch, E. D.; Murray, L. J.; Queen, W. L.; Chavan, S.; Maximoff, S. N.; Bigi, J. P.; Krishna, R.; Peterson, V. K.; Grandjean, F.; Long, G. J.; Smit, B.; Bordiga, S.; Brown, C. M.; Long, J. R. Selective Binding of O2 over N2 in a Redox–Active Metal–Organic Framework with Open Iron(II) Coordination Sites. *J. Am. Chem. Soc.* **2011**, *133* (37), 14814–14822. https://doi.org/10.1021/ja205976v.

30 Severin, K. Synthetic Chemistry with Nitrous Oxide. *Chem. Soc. Rev.* **2015**, *44* (17), 6375–6386. https://doi.org/10.1039/C5CS00339C.

31 Parmon, V. N.; Panov, G. I.; Uriarte, A.; Noskov, A. S. Nitrous Oxide in Oxidation Chemistry and Catalysis: Application and Production. *Catalysis Today* **2005**, *100* (1–2), 115–131. https://doi.org/10.1016/j.cattod.2004.12.012.

32 Le Vaillant, F.; Mateos Calbet, A.; González-Pelayo, S.; Reijerse, E. J.; Ni, S.; Busch, J.; Cornella, J. Catalytic Synthesis of Phenols with Nitrous Oxide. *Nature* **2022**, *604* (7907), 677–683. https://doi.org/10.1038/s41586-022-04516-4.

33 Bols, M. L.; Snyder, B. E. R.; Rhoda, H. M.; Cnudde, P.; Fayad, G.; Schoonheydt, R. A.; Van Speybroeck, V.; Solomon, E. I.; Sels, B. F. Coordination and Activation of Nitrous Oxide by Iron Zeolites. *Nat. Catal.* **2021**, *4* (4), 332–340. https://doi.org/10.1038/s41929-021-00602-4.

34 Simons, M. C.; Prinslow, S. D.; Babucci, M.; Hoffman, A. S.; Hong, J.; Vitillo, J. G.; Bare, S. R.; Gates, B. C.; Lu, C. C.; Gagliardi, L.; Bhan, A. Beyond Radical Rebound: Methane Oxidation to Methanol Catalyzed by Iron Species in Metal–Organic Framework Nodes. *J. Am. Chem. Soc.* **2021**, *143* (31), 12165–12174. https://doi.org/10.1021/jacs.1c04766.

35 Barona, M.; Ahn, S.; Morris, W.; Hoover, W.; Notestein, J. M.; Farha, O. K.; Snurr, R. Q. Computational Predictions and Experimental Validation of Alkane Oxidative Dehydrogenation by Fe2M MOF Nodes. *ACS Catal.* **2020**, *10* (2), 1460–1469. https://doi.org/10.1021/acscatal.9b03932.

36 Xiao, D. J.; Bloch, E. D.; Mason, J. A.; Queen, W. L.; Hudson, M. R.; Planas, N.; Borycz, J.; Dzubak, A. L.; Verma, P.; Lee, K.; Bonino, F.; Crocellà, V.; Yano, J.; Bordiga, S.; Truhlar, D. G.; Gagliardi, L.; Brown, C. M.; Long, J. R. Oxidation of Ethane to Ethanol by N2O in a Metal–Organic Framework with Coordinatively Unsaturated Iron(II) Sites. *Nat. Chem.* **2014**, *6* (7), 590–595. https://doi.org/10.1038/nchem.1956.

37 Tofoni, A.; Tavani, F.; Vandone, M.; Braglia, L.; Borfecchia, E.; Ghigna, P.; Stoian, D. C.; Grell, T.; Stolfi, S.; Colombo, V.; D'Angelo, P. Full Spectroscopic Characterization of the Molecular Oxygen-Based Methane to Methanol Conversion over Open Fe(II) Sites in a Metal–Organic Framework. *J. Am. Chem. Soc.* **2023**, jacs.3c07216. https://doi.org/10.1021/jacs.3c07216.

38 Vitillo, J. G.; Choudhary, M.; Simons, M. C.; Gagliardi, L.; Bhan, A. Mechanism of Benzene Hydroxylation on Tri-Iron Oxo-Centered Cluster-Based Metal–Organic Frameworks. *J. Phys. Chem. C* **2023**, acs.jpcc.3c06423. https://doi.org/10.1021/acs.jpcc.3c06423.

39 Verma, P.; Vogiatzis, K. D.; Planas, N.; Borycz, J.; Xiao, D. J.; Long, J. R.; Gagliardi, L.; Truhlar, D. G. Mechanism of Oxidation of Ethane to Ethanol at Iron(IV)–Oxo Sites in Magnesium-Diluted Fe2(dobdc). *J. Am. Chem. Soc.* **2015**, *137* (17), 5770–5781. https://doi.org/10.1021/jacs.5b00382.

40 Borycz, J.; Paier, J.; Verma, P.; Darago, L. E.; Xiao, D. J.; Truhlar, D. G.; Long, J. R.; Gagliardi, L. Structural and Electronic Effects on the Properties of Fe2(dobdc) upon Oxidation with N2O. *Inorg. Chem.* **2016**, *55* (10), 4924–4934. https://doi.org/10.1021/acs.inorgchem.6b00467.

41 Suh, B. L.; Kim, J. Ligand Insertion in MOF-74 as Effective Design for Oxidation of Ethane to Ethanol. *J. Phys. Chem. C* **2018**, *122* (40), 23078–23083.

42 Costas, M.; Mehn, M. P.; Jensen, M. P.; Que, L. Dioxygen Activation at Mononuclear Nonheme Iron Active Sites: Enzymes, Models, and Intermediates. *Chem. Rev.* **2004**, *104* (2), 939–986. https://doi.org/10.1021/cr020628n.

43 Wallar, B. J.; Lipscomb, J. D. Dioxygen Activation by Enzymes Containing Binuclear Non-Heme Iron Clusters. *Chem. Rev.* **1996**, *96* (7), 2625–2658. https://doi.org/10.1021/cr9500489.

44 Meunier, B.; De Visser, S. P.; Shaik, S. Mechanism of Oxidation Reactions Catalyzed by Cytochrome P450 Enzymes. *Chem. Rev.* **2004**, *104* (9), 3947–3980. https://doi.org/10.1021/cr020443g.

45 Zhuravlev, V.; Malinowski, P. J. A Stable Crystalline Copper(I)–N2O Complex Stabilized as the Salt of a Weakly Coordinating Anion. *Angew. Chem. Int. Ed.* **2018**, *57* (36), 11697–11700. https://doi.org/10.1002/anie.201806836.

46 Mokhtarzadeh, C. C.; Chan, C.; Moore, C. E.; Rheingold, A. L.; Figueroa, J. S. Side-On Coordination of Nitrous Oxide to a Mononuclear Cobalt Center. *J. Am. Chem. Soc.* **2019**, *141* (38), 15003–15007. https://doi.org/10.1021/jacs.9b08241.

47 Piro, N. A.; Lichterman, M. F.; Harman, W. H.; Chang, C. J. A Structurally Characterized Nitrous Oxide Complex of Vanadium. *J. Am. Chem. Soc.* **2011**, *133* (7), 2108–2111. https://doi.org/10.1021/ja110798w.

48 Pamplin, C. B.; Ma, E. S. F.; Safari, N.; Rettig, S. J.; James, B. R. The Nitrous Oxide Complex RuCl2(η^1-N2O)(P-N)(PPh3) (P-N = [o-(N,N-Dimethylamino)phenyl]diphenylphosphine); Low Temperature Conversion of N2O to N2 and O2. *J. Am. Chem. Soc.* **2001**, *135* (35), 8596–8597. https://doi.org/10.1021/ja0106319.

49 Paulat, F.; Kuschel, T.; Näther, C.; Praneeth, V. K. K.; Sander, O.; Lehnert, N. Spectroscopic Properties and Electronic

Structure of Pentammineruthenium(II) Dinitrogen Oxide and Corresponding Nitrosyl Complexes: Binding Mode of N_2O and Reactivity. *Inorg. Chem.* **2004**, *43* (22), 6979–6994. https://doi.org/10.1021/ic049302i.

50 Puerta Lombardi, B.; Gendy, C.; Gelfand, B. S.; Bertrand, G. M.; Wasylishen, R. E.; Tuononen, H. M.; Roesler, R. Side-on Coordination in Isostructural Nitrous Oxide and Carbon Dioxide Complexes of Nickel. *Angew. Chem. Int. Ed. 60* (13), 7077–7081. https://doi.org/10.1002/anie.202011301.

51 Gyton, M. R.; Leforestier, B.; Chaplin, A. B. Rhodium(I) Pincer Complexes of Nitrous Oxide. *Angewandte Chemie* **2019**, *131* (43), 15439–15442. https://doi.org/10.1002/ange.201908333.

52 Tolman, W. B. Binding and Activation of N_2O at Transition-Metal Centers: Recent Mechanistic Insights. *Angew. Chem. Int. Ed.* **2010**, *49* (6), 1018–1024. https://doi.org/10.1002/anie.200905364.

53 Ketrat, S.; Maihom, T.; Wannakao, S.; Probst, M.; Nokbin, S.; Limtrakul, J. Coordinatively Unsaturated Metal–Organic Frameworks $M_3(btc)_2$ (M = Cr, Fe, Co, Ni, Cu, and Zn) Catalyzing the Oxidation of CO by N_2O: Insight from DFT Calculations. *Inorg. Chem.* **2017**, *56* (22), 14005–14012. https://doi.org/10.1021/acs.inorgchem.7b02143.

54 Rieth, A. J.; Wright, A. M.; Skorupskii, G.; Mancuso, J. L.; Hendon, C. H.; Dincă, M. Record-Setting Sorbents for Reversible Water Uptake by Systematic Anion Exchanges in Metal–Organic Frameworks. *J. Am. Chem. Soc.* **2019**, *141* (35), 13858–13866. https://doi.org/10.1021/jacs.9b06246.

55 Zick, M. E.; Lee, J.-H.; Gonzalez, M. I.; Velasquez, E. O.; Uliana, A. A.; Kim, J.; Long, J. R.; Milner, P. J. Fluoroarene Separations in Metal–Organic Frameworks with Two Proximal Mg^{2+} Coordination Sites. *J. Am. Chem. Soc.* **2021**, *143* (4), 1948–1958. https://doi.org/10.1021/jacs.0c11530.

56 Geier, S. J.; Mason, J. A.; Bloch, E. D.; Queen, W. L.; Hudson, M. R.; Brown, C. M.; Long, J. R. Selective Adsorption of Ethylene over Ethane and Propylene over Propane in the Metal–Organic Frameworks $M_2(dobdc)$ (M = Mg, Mn, Fe, Co, Ni, Zn). *Chem. Sci.* **2013**, *4* (5), 2054–2061. https://doi.org/10.1039/c3sc00032j.

57 Gonzalez, M. I.; Kapelewski, M. T.; Bloch, E. D.; Milner, P. J.; Reed, D. A.; Hudson, M. R.; Mason, J. A.; Barin, G.; Brown, C. M.; Long, J. R. Separation of Xylene Isomers through Multiple Metal Site Interactions in Metal–Organic Frameworks. *J. Am. Chem. Soc.* **2018**, *140* (9), 3412–3422. https://doi.org/10.1021/jacs.7b13825.

58 Mason, J. A.; Veenstra, M.; Long, J. R. Evaluating Metal–Organic Frameworks for Natural Gas Storage. *Chem. Sci.* **2014**, *5* (1), 32–51. https://doi.org/10.1039/C3SC52633J.

59 Sumida, K.; Stück, D.; Mino, L.; Chai, J.-D.; Bloch, E. D.; Zavorotynska, O.; Murray, L. J.; Dincă, M.; Chavan, S.; Bordiga, S.; Head-Gordon, M.; Long, J. R. Impact of Metal and Anion Substitutions on the Hydrogen Storage Properties of M-BTT Metal–Organic Frameworks. *J. Am. Chem. Soc.* **2013**, *135* (3), 1083–1091. https://doi.org/10.1021/ja310173e.

60 Irving, H.; Williams, R. J. P. Order of Stability of Metal Complexes. *Nature* **1948**, *162*, 746–747. https://doi.org/10.1038/162746a0.

61 Yu, D.; Yazaydin, A. O.; Lane, J. R.; Dietzel, P. D. C.; Snurr, R. Q. A Combined Experimental and Quantum Chemical Study of CO_2 Adsorption in the Metal–Organic Framework CPO-27 with Different Metals. *Chem. Sci.* **2013**, *4* (9), 3544–3556. https://doi.org/10.1039/c3sc51319j.

62 Rosnes, M. H.; Sheptyakov, D.; Franz, A.; Frontzek, M.; Dietzel, P. D. C.; Georgiev, P. A. On the Elusive Nature of Oxygen Binding at Coordinatively Unsaturated 3d Transition Metal Centers in Metal–Organic Frameworks. *Phys. Chem. Chem. Phys.* **2017**, *19* (38), 26346–26357. https://doi.org/10.1039/C7CP05119K.

63 Barona, M.; Snurr, R. Q. Exploring the Tunability of Trimetallic MOF Nodes for Partial Oxidation of Methane to Methanol. *ACS Appl. Mater. Interfaces* **2020**, *12* (25), 28217–28231. https://doi.org/10.1021/acsami.0c06241.

64 Zhang, Q.; Li, B.; Chen, L. First-Principles Study of Microporous Magnets M-MOF-74 (M = Ni, Co, Fe, Mn): The Role of Metal Centers. *Inorg. Chem.* **2013**, *52* (16), 9356–9362. https://doi.org/10.1021/ic400927m.

65 Bloch, E. D.; Queen, W. L.; Krishna, R.; Zadrozny, J. M.; Brown, C. M.; Long, J. R. Hydrocarbon Separations in a Metal-Organic Framework with Open Iron(II) Coordination Sites. *Science* **2012**, *335* (6076), 1606–1610. https://doi.org/10.1126/science.1217544.

66 Vogiatzis, K. D.; Haldoupis, E.; Xiao, D. J.; Long, J. R.; Siepmann, J. I.; Gagliardi, L. Accelerated Computational Analysis of Metal–Organic Frameworks for Oxidation Catalysis. *J. Phys. Chem. C* **2016**, *120* (33), 18707–18712. https://doi.org/10.1021/acs.jpcc.6b07115.

67 Vitillo, J. G.; Lu, C. C.; Cramer, C. J.; Bhan, A.; Gagliardi, L. Influence of First and Second Coordination Environment on Structural Fe(II) Sites in MIL-101 for C–H Bond Activation in Methane. *ACS Catal.* **2021**, *11* (2), 579–589. https://doi.org/10.1021/acscatal.0c03906.

68 Larson, V. A.; Battistella, B.; Ray, K.; Lehnert, N.; Nam, W. Iron and Manganese Oxo Complexes, Oxo Wall and Beyond. *Nat. Rev. Chem.* **2020**, *4* (8), 404–419. https://doi.org/10.1038/s41570-020-0197-9.

69 Yamashita, T.; Vannice, A. N_2O Decomposition over Manganese Oxides. *Journal of Catalysis* **1996**, *161* (1), 254–262. https://doi.org/10.1006/jcat.1996.0183.

70 Ross, R. A.; Fairbridge, C. Oxidation of 1-Butene by Nitrous Oxide over Manganese(III) and Related Transition Metal Oxides. *Can. J. Chem.* **1984**, *62* (8), 1483–1486. https://doi.org/10.1139/v84-252.

71 Ben-Daniel, R.; Weiner, L.; Neumann, R. Activation of Nitrous Oxide and Selective Epoxidation of Alkenes Catalyzed by the Manganese-Substituted Polyoxometalate, $[Mn^{III}_2ZnW(Zn_2W_9O_{34})_2]^{10-}$. *J. Am. Chem. Soc.* **2002**, *124* (30), 8788–8789. https://doi.org/10.1021/ja0259077.

72 Jiang, M.-X.; Liu, C.-G. New Insight into the Catalytic Cycle about Epoxidation of Alkenes by N_2O over a Mn–Substituted Keggin-Type Polyoxometalate. *Journal of Molecular Graphics and Modelling* **2017**, *73*, 8–17. https://doi.org/10.1016/j.jmgm.2016.12.012.

73 Li, Y.; Armor, J. N. Catalytic Decomposition of Nitrous Oxide on Metal Exchanged Zeolites. *Appl. Catal. B* **1992**, *1* (3), L21–L29. https://doi.org/10.1016/0926-3373(92)80019-V.

74 Campa, M. C.; Indovina, V.; Pietrogiacomi, D. The Selective Catalytic Reduction of N_2O with CH_4 on Na-MOR and Na-MFI Exchanged with Copper, Cobalt or Manganese. *Applied Catalysis B: Environmental* **2012**, *111–112*, 90–95. https://doi.org/10.1016/j.apcatb.2011.09.021.

75 Cozzolino, A. F.; Brozek, C. K.; Palmer, R. D.; Yano, J.; Li, M.; Dincă, M. Ligand Redox Non-Innocence in the Stoichiometric Oxidation of $Mn_2(2,5-dioxidoterephthalate)$ (Mn-MOF-74). *J. Am. Chem. Soc.* **2014**, *136* (9), 3334–3337. https://doi.org/10.1021/ja411808r.

76 Halbach, R. L.; Gygi, D.; Bloch, E. D.; Anderson, B. L.; Nocera, D. G. Structurally Characterized Terminal Manganese(IV) Oxo Tris(Alkoxide) Complex. *Chem. Sci.* **2018**, *9* (19), 4524–4528. https://doi.org/10.1039/C8SC01164H.

77 Wang, X.; Andrews, L. Infrared Spectra of $M(OH)_{1,2,3}$ (M = Mn, Fe, Co, Ni) Molecules in Solid Argon and the Character of First Row Transition Metal Hydroxide Bonding. *J. Phys. Chem. A* **2006**, *110* (33), 10035–10045. https://doi.org/10.1021/jp0624698.

78 Canivet, J.; Fateeva, A.; Guo, Y.; Coasne, B.; Farrusseng, D. Water Adsorption in MOFs: Fundamentals and Applications.

Chem.   Soc.   Rev. **2014**, *43* (16),   5594–5617. https://doi.org/10.1039/C4CS00078A.